International Journal of Heat and Fluid Flow 56 (2015) 261–271

Contents lists available at ScienceDirect

International Journal of Heat and Fluid Flow

journal homepage: www.elsevier.com/locate/ijhff

A three-dimensional pseudo-potential-based lattice Boltzmann model for multiphase flows with large density ratio and variable surface tension

A. Xu, T.S. Zhao *, L. An, L. Shi

Department of Mechanical and Aerospace Engineering, The Hong Kong University of Science and Technology, Clear Water Bay, Kowloon, Hong Kong Special Administrative Region

ARTICLE INFO

Article history:
Received 30 April 2015
Received in revised form 11 August 2015
Accepted 11 August 2015

Keywords:
Lattice Boltzmann method
Multiphase flow
Three dimension
Large density ratio
Variable surface tension

ABSTRACT

In this paper, we present a three-dimensional pseudo-potential-based lattice Boltzmann (LB) model with an improved forcing scheme for multiphase flows. The Chapman–Enskog multiscale analysis shows that the proposed forcing scheme allows the lattice Boltzmann equation to recover the three-dimensional hydrodynamical equations with additional terms that correspond to the mechanical stability condition and surface tension. Validations of the present LB model with Maxwell construction, Laplace's law and oscillation dynamics demonstrate that the model enables the density ratio to be as large as 700 in static and quasi-static cases while maintaining variable surface tension. Finally, the application of the model to simulation of the droplet motion in a microchannel shows that the model allows the analysis of important effects, including droplet surface tension, channel surface wettability, and channel surface roughness.

1. Introduction

A great deal of numerical studies on multiphase flows have been done during the past decades, and they have attracted much attention recently because of their wide applications in microfluidics devices (Cheng et al., 2014). Traditionally, multiphase flows are simulated by solving the macroscopic Navier–Stokes equations coupled with various approaches to track the interface among different phases. Generally, these approaches are classified into two categories: one is the interface-tracking approach, i.e., using Lagrangian approach to explicitly represent the interface, such as the front tracking method (Unverdi and Tryggvason, 1992), while the other is the interface-capturing approach, i.e., using Eulerian approach to implicitly represent the interface by a scalar function, such as the volume of fluid method (Hirt and Nichols, 1981), the level set method (Sethian and Smereka, 2003), and the phase field method (Badalassi et al., 2003). However, simulation of multiphase flows based on the Navier–Stokes equations remains a challenging issue as it is difficult to track complex phase interfaces that physically result from microscopic interactions between molecules (Sbragaglia et al., 2006).

Alternatively, due to its kinetic nature, the lattice Boltzmann (LB) method has proved to be a promising tool for simulating fluid systems involving interfacial dynamics (such as multiphase flows) and complex boundaries (such as porous media) (Chen and Doolen, 1998). Existing LB models for multiphase flows can be generally classified into four categories: the color-gradient model (Gunstensen et al., 1991; Grunau et al., 1993), the pseudo-potential model (Shan and Chen, 1993; Shan and Chen, 1994), the free-energy model (Swift et al., 1995; Swift et al., 1996), and the kinetic-theory-based model (He et al., 1998; He and Doolen, 2002). Among those models, the pseudo-potential model, which is also called Shan–Chen model, has received much attention, primarily because interfaces can naturally arise, deform, and migrate, thereby improving the computational efficiency (Chen et al., 2014; Succi, 2015). Specifically, the fluid interactions are described by an artificial inter-particle potential and the phase separation is naturally achieved by imposing a short-range attraction among different phases. However, there are two issues associated with the pseudo-potential model proposed by Shan and Chen (1993, 1994). One is that this model is applicable to low-density-ratio interfacial problems only (Yuan and Schaefer, 2006), while the other is that in this model surface tension cannot be varied independently of the density ratio (Sbragaglia et al., 2007). Over the past years, efforts have been made to address these issues (Yuan and Schaefer, 2006; Sbragaglia et al., 2007; Shan, 2006; Huang et al., 2011; Li et al., 2012; Li et al., 2013; Li and Luo, 2013). For

* Corresponding author. Tel.: +852 2358 8647.
E-mail address: metzhao@ust.hk (T.S. Zhao).

http://dx.doi.org/10.1016/j.ijheatfluidflow.2015.08.001
0142-727X/

instance, one of previous efforts is to incorporate the fluid interaction force into the pseudo-potential model via improving the forcing scheme (Huang et al., 2011; Li et al., 2012; Li et al., 2013; Li and Luo, 2013). Li et al. (2013) proposed a forcing scheme for a two-dimensional (2D) multiple-relaxation-time (MRT) pseudo-potential LB model. This forcing scheme can adjust the mechanical stability condition so that multiphase flows with a large density ratio can be simulated. In addition, Li and Luo (2013) also proposed to adjust the surface tension in the 2D MRT pseudo-potential LB model by incorporating a source term of the LB equation, which is based on the derivation of discrete form pressure tensor. As a practical numerical tool for simulating engineering problems, however, it is desirable to extend 2D models to three-dimensional (3D) models to truly reflect the real-world multiphase flow behaviors. However, as the underlying lattice structure for 2D and 3D models are different, there are significant differences in the development and implementation of 3D MRT models (Premnath and Abraham, 2007).

In this work, we extend the 2D forcing scheme proposed by Li et al. (2013) and Li and Luo (2013) to 3D MRT pseudo-potential LB model for single-component multiphase flows with a large density ratio and variable surface tension. The rest of the paper is organized as follows: In Section 2, we present the pseudo-potential LB model and give the new forcing scheme, followed by the Chapman–Enskog analysis to derive macroscopic equations. In Section 3, the present multiphase LB model is evaluated by verifying Maxwell construction, Laplace's law, spurious velocities, spatial accuracy, oscillation dynamics and contact angle, respectively. After that, numerical simulations are carried out to study liquid droplets moving in a 3D microchannel, including the effects of droplet surface tension, channel surface wettability, and channel surface roughness.

2. Numerical method

2.1. Two-phase lattice Boltzmann method

2.1.1. The multiple-relaxation-time LB model

The evolution equation of LB model can be written as

$$f_i(\mathbf{x}+\mathbf{e}_i\delta_t, t+\delta_t) - f_i(\mathbf{x},t) = \Omega_i + \delta_t F_i' \tag{1}$$

where f_i is the density distribution function, t is the time, $\mathbf{x}$ is particle position, $\mathbf{e}_i$ is the discrete velocity along the ith direction, δ_t is the time step, F_i' is the forcing term in velocity space, Ω_i is the collision operator which can be expressed by either Bhatnagar–Gross–Krook (BGK) collision operator (Qian et al., 1992) or multiple-relaxation-time (MRT) collision operator (Lallemand and Luo, 2000; d'Humières, 2002). In this work, we adopt MRT collision operator for its superior numerical stability over BGK collision operator in simulating both single and multiphase flow (Premnath and Abraham, 2007; Lallemand and Luo, 2000; d'Humières, 2002; Chai and Zhao, 2012). The MRT collision operator Ω_i is defined as

$$\Omega_i = -(\mathbf{M}^{-1}\mathbf{S}\mathbf{M})_{ij}\left[f_j(\mathbf{x},t) - f_j^{(\mathrm{eq})}(\mathbf{x},t)\right] \tag{2}$$

For the D3Q15 lattice model, $\mathbf{e}_i$ can be given as

$$[\mathbf{e}_0,\mathbf{e}_1,\mathbf{e}_2,\mathbf{e}_3,\mathbf{e}_4,\mathbf{e}_5,\mathbf{e}_6,\mathbf{e}_7,\mathbf{e}_8,\mathbf{e}_9,\mathbf{e}_{10},\mathbf{e}_{11},\mathbf{e}_{12},\mathbf{e}_{13},\mathbf{e}_{14}] = c\begin{bmatrix} 0 & 1 & -1 & 0 & 0 & 0 & 0 & 1 & -1 & 1 & -1 & 1 & -1 & 1 & -1 \\ 0 & 0 & 0 & 1 & -1 & 0 & 0 & 1 & 1 & -1 & -1 & 1 & 1 & -1 & -1 \\ 0 & 0 & 0 & 0 & 0 & 1 & -1 & 1 & 1 & 1 & 1 & -1 & -1 & -1 & -1 \end{bmatrix} \tag{3}$$

where $c = \delta_x/\delta_t$ is lattice constant. $\mathbf{M}$ is orthogonal transformation matrix, given by d'Humières (2002)

$$\mathbf{M} = \begin{bmatrix} 1 & 1 & 1 & 1 & 1 & 1 & 1 & 1 & 1 & 1 & 1 & 1 & 1 & 1 & 1 \\ -2 & -1 & -1 & -1 & -1 & -1 & -1 & 1 & 1 & 1 & 1 & 1 & 1 & 1 & 1 \\ 16 & -4 & -4 & -4 & -4 & -4 & -4 & 1 & 1 & 1 & 1 & 1 & 1 & 1 & 1 \\ 0 & 1 & -1 & 0 & 0 & 0 & 0 & 1 & -1 & 1 & -1 & 1 & -1 & 1 & -1 \\ 0 & -4 & 4 & 0 & 0 & 0 & 0 & 1 & -1 & 1 & -1 & 1 & -1 & 1 & -1 \\ 0 & 0 & 0 & 1 & -1 & 0 & 0 & 1 & 1 & -1 & -1 & 1 & 1 & -1 & -1 \\ 0 & 0 & 0 & -4 & 4 & 0 & 0 & 1 & 1 & -1 & -1 & 1 & 1 & -1 & -1 \\ 0 & 0 & 0 & 0 & 0 & 1 & -1 & 1 & 1 & 1 & 1 & -1 & -1 & -1 & -1 \\ 0 & 0 & 0 & 0 & 0 & -4 & 4 & 1 & 1 & 1 & 1 & -1 & -1 & -1 & -1 \\ 0 & 2 & 2 & -1 & -1 & -1 & -1 & 0 & 0 & 0 & 0 & 0 & 0 & 0 & 0 \\ 0 & 0 & 0 & 1 & 1 & -1 & -1 & 0 & 0 & 0 & 0 & 0 & 0 & 0 & 0 \\ 0 & 0 & 0 & 0 & 0 & 0 & 0 & 1 & -1 & -1 & 1 & 1 & -1 & -1 & 1 \\ 0 & 0 & 0 & 0 & 0 & 0 & 0 & 1 & 1 & -1 & -1 & -1 & -1 & 1 & 1 \\ 0 & 0 & 0 & 0 & 0 & 0 & 0 & 1 & -1 & 1 & -1 & -1 & 1 & -1 & 1 \\ 0 & 0 & 0 & 0 & 0 & 0 & 0 & 1 & -1 & -1 & 1 & -1 & 1 & 1 & -1 \end{bmatrix} \tag{4}$$

and $\mathbf{S}$ is a relaxation matrix. To keep the relaxation matrix $\mathbf{S}$ consistent with the moment, we write it as $\mathbf{S} = \mathrm{diag}(s_\rho, s_e, s_\epsilon, s_j, s_q, s_j, s_q, s_j, s_q, s_v, s_v, s_v, s_v, s_v, s_{xyz})$.

The density distribution function f_i and its equilibrium distribution $f_i^{(\mathrm{eq})}$ can be projected onto moment space via $\mathbf{m} = \mathbf{M}\mathbf{f}$ and $\mathbf{m}^{(\mathrm{eq})} = \mathbf{M}\mathbf{f}^{(\mathrm{eq})}$, respectively. Thus, the evolution equation of density distribution function can be rewritten as

$$\mathbf{m}^* = \mathbf{m} - \mathbf{S}(\mathbf{m} - \mathbf{m}^{(\mathrm{eq})}) + \delta_t\left(\mathbf{I} - \frac{\mathbf{S}}{2}\right)\mathbf{M}\tilde{\mathbf{F}} \tag{5}$$

where $\mathbf{I}$ is the unit tensor and $\mathbf{M}\tilde{\mathbf{F}}$ is the forcing term in the moment space with $(\mathbf{I} - 0.5\mathbf{S})\mathbf{M}\tilde{\mathbf{F}} = \mathbf{M}\mathbf{F}'$, the equilibrium $\mathbf{m}^{(\mathrm{eq})}$ is given by

$$\mathbf{m}^{(\mathrm{eq})} = \rho\left(1, -1 + |\mathbf{u}|^2, 1 - 5|\mathbf{u}|^2, u_x, -\frac{7}{3}u_x, u_y, -\frac{7}{3}u_y, u_z, -\frac{7}{3}u_z, 2u_x^2 - u_y^2 - u_z^2, u_y^2 - u_z^2, u_xu_y, u_yu_z, u_xu_z, 0\right)^T \tag{6}$$

where u_x, u_y and u_z denote the fluid velocity components in the (x,y,z) Cartesian coordinate system, and $|\mathbf{u}|^2 = u_x^2 + u_y^2 + u_z^2$.

The macroscopic density ρ and velocity $\mathbf{u}$ are obtained from

$$\rho = \sum_i f_i, \quad \rho\mathbf{u} = \sum_i \mathbf{e}_i f_i + \frac{\delta_t}{2}\mathbf{F} \tag{7}$$

where $\mathbf{F} = (F_x, F_y, F_z)$ is the total force acting on the system.

2.1.2. Pseudo-potential model

For single-component multiphase flows, the interaction force mimicking molecular interactions, is given by Shan (2006, 2008)

$$\mathbf{F}_{\mathrm{int}}(\mathbf{x}) = -G\psi(\mathbf{x})\sum_{i=1}^{N} w(|\mathbf{e}_i|^2)\psi(\mathbf{x}+\mathbf{e}_i)\mathbf{e}_i \tag{8}$$

where $\psi(\mathbf{x})$ is the interaction potential, G is the interaction strength, and $w(|\mathbf{e}_i|^2)$ are the weights. For the case of nearest-neighbor interactions on D3Q15 lattice, $w(1) = 1/3$, $w(3) = 1/24$ and $N = 14$.

In the pseudo-potential model, the interaction force is usually incorporated via a forcing scheme, which affects the numerical accuracy and stability of the model. In this study, we extend the forcing scheme proposed by Li et al. (2013) and Li and Luo (2013) to D3Q15 lattice. The evolution equation of density distribution function is written as

$$\mathbf{m}^* = \mathbf{m} - \mathbf{S}(\mathbf{m} - \mathbf{m}^{(\mathrm{eq})}) + \delta_t\left(\mathbf{I} - \frac{\mathbf{S}}{2}\right)\mathbf{M}\tilde{\mathbf{F}} + \mathbf{C} \tag{9}$$

where the term $\mathbf{M}\tilde{\mathbf{F}}$ and $\mathbf{C}$ are given by

$$\mathbf{M}\tilde{\mathbf{F}}=\begin{bmatrix}0\\ 2\mathbf{u}\cdot\mathbf{F}+\frac{6\sigma|\mathbf{F}|^2}{\psi^2\delta_t(s_e^{-1}-0.5)}\\ -10\mathbf{u}\cdot\mathbf{F}\\ F_x\\ -\frac{7}{3}F_x\\ F_y\\ -\frac{7}{3}F_y\\ F_z\\ -\frac{7}{3}F_z\\ 4u_xF_x-2u_yF_y-2u_zF_z\\ 2u_yF_y-2u_zF_z\\ u_xF_y+u_yF_x\\ u_yF_z+u_zF_y\\ u_xF_z+u_zF_x\\ 0\end{bmatrix},\quad \mathbf{C}=\begin{bmatrix}0\\ \frac{4}{5}s_e(Q_{xx}+Q_{yy}+Q_{zz})\\ 0\\ 0\\ 0\\ 0\\ 0\\ 0\\ 0\\ -s_v(2Q_{xx}-Q_{yy}-Q_{zz})\\ -s_v(Q_{yy}-Q_{zz})\\ -s_vQ_{xy}\\ -s_vQ_{yz}\\ -s_vQ_{xz}\\ 0\end{bmatrix} \tag{10}$$

respectively. Here, σ is used to vary the mechanical stability condition. The variables Q_{xx}, Q_{yy}, Q_{zz}, Q_{xy}, Q_{yz} and Q_{xz} are obtained from

$$\mathbf{Q}=\kappa\frac{G}{2}\psi(\mathbf{x})\sum_{i=1}^{14}w(|\mathbf{e}_i|^2)[\psi(\mathbf{x}+\mathbf{e}_i)-\psi(\mathbf{x})]\mathbf{e}_i\mathbf{e}_i \tag{11}$$

where the parameter κ is used to vary the surface tension.

2.1.3. Fluid–solid interactions

When a solid wall is encountered, the adhesive force between the solid and the fluid should also be considered (Martys and Chen, 1996). Historically, two widely used fluid–solid interaction have been proposed: the density-based interaction (Martys and Chen, 1996; Kang et al., 2002) and the pseudopotential-based interaction (Raiskinmäki et al., 2000; Benzi et al., 2006).

Recently, Li et al. (2014) studied the implementation of contact angles in the pseudo-potential LB model at a large density ratio, and formulated a modified pseudopotential-based fluid–solid interaction, given by

$$\mathbf{F}_{\text{ads}}(\mathbf{x})=-G_{\text{ads}}\psi(\mathbf{x})\sum_i w(|\mathbf{e}_i|^2)\psi(\mathbf{x})s(\mathbf{x}+\mathbf{e}_i)\mathbf{e}_i \tag{12}$$

where G_{ads} is the fluid–solid interaction strength for adjusting the contact angles. $s(\mathbf{x})$ is the indicator function, $s(\mathbf{x})=1$ when $\mathbf{x}$ is in solid and $s(\mathbf{x})=0$ when $\mathbf{x}$ is in fluid.

With the body force $\mathbf{F}_{\text{body}}$, the total force $\mathbf{F}$ in Eq. (10) is given by

$$\mathbf{F}=\mathbf{F}_{\text{int}}+\mathbf{F}_{\text{ads}}+\mathbf{F}_{\text{body}} \tag{13}$$

2.2. Derivation of the macroscopic equations

We now present a detailed analysis of the derivation of the macroscopic equations for multiphase flows from LB equation with the above proposed forcing scheme. To this end, we adopt the Chapman–Enskog analysis (Chai and Zhao, 2012).

Applying Taylor expansions for Eq. (9) to second-order, we obtain

$$\hat{\mathbf{D}}\mathbf{m}+\frac{\delta_t}{2}\hat{\mathbf{D}}^2\mathbf{m}=-\mathbf{S}'(\mathbf{m}-\mathbf{m}^{(\text{eq})})+\left(\mathbf{I}-\frac{\mathbf{S}}{2}\right)\mathbf{M}\tilde{\mathbf{F}}+\frac{1}{\delta_t}\tilde{\mathbf{C}} \tag{14}$$

where $\hat{\mathbf{D}}=\mathbf{M}\mathbf{D}\mathbf{M}^{-1}$, $\mathbf{D}=\partial_t\mathbf{I}+\partial_\alpha\text{diag}(c_{0\alpha},c_{1\alpha},\ldots,c_{14\alpha})$, and $\mathbf{S}'=\mathbf{S}/\delta_t$. Introduce the following multiscale expansions,

$$\begin{aligned}&\mathbf{m}=\sum_{n=0}^{\infty}\epsilon^n\mathbf{m}^{(n)},\ \partial_t=\epsilon\partial_{t_1}+\epsilon^2\partial_{t_2},\ \partial_\alpha=\epsilon\partial_{\alpha_1},\\ &\mathbf{F}=\epsilon\mathbf{F}_1,\ \mathbf{C}=\epsilon\mathbf{C}_1\end{aligned} \tag{15}$$

where $\mathbf{m}^k=\mathbf{M}\cdot\mathbf{f}^{(k)}$, $\mathbf{F}_1=(F_{x_1},F_{y_1},F_{z_1})$.

Substituting the above expansions into Eq. (14), we can obtain the zero-, first-, and second-order equations in ϵ as

$$\epsilon^0:\ \mathbf{m}^{(0)}=\mathbf{m}^{(\text{eq})} \tag{16a}$$

$$\epsilon^1:\ \hat{\mathbf{D}}_1\mathbf{m}^{(0)}=-\mathbf{S}'\mathbf{m}^{(1)}+\left(\mathbf{I}-\frac{\mathbf{S}}{2}\right)\mathbf{M}\tilde{\mathbf{F}}_1+\frac{1}{\delta_t}\mathbf{C}_1 \tag{16b}$$

$$\begin{aligned}\epsilon^2:\ &\partial_{t_2}\mathbf{m}^{(0)}+\hat{\mathbf{D}}_1(\mathbf{I}-\frac{\mathbf{S}}{2})\mathbf{m}^{(1)}+\frac{\delta_t}{2}\hat{\mathbf{D}}_1\left(\mathbf{I}-\frac{\mathbf{S}}{2}\right)\mathbf{M}\tilde{\mathbf{F}}_1\\ &+\frac{1}{2}\hat{\mathbf{D}}_1\mathbf{C}_1=-\mathbf{S}'\mathbf{m}^{(2)}\end{aligned} \tag{16c}$$

where $\mathbf{S}'=\mathbf{S}/\delta_t$, $\hat{\mathbf{D}}_1=\mathbf{M}\mathbf{D}_1\mathbf{M}^{-1}$, and $\mathbf{D}_1=\partial_{t_1}\mathbf{I}+\partial_{\alpha_1}\text{diag}(c_{0\alpha},c_{1\alpha},\ldots,c_{14\alpha})$. The elements of $\mathbf{m}^{(1)}$ corresponding to the conservative variables ρ and $\rho\mathbf{u}$ are zero and $-\delta_t\mathbf{F}_1/2$, so we can further rewrite Eq. (16) as

$$\begin{aligned}&\partial_{t_1}\begin{bmatrix}\rho\\ \rho(-1+|\mathbf{u}|^2)\\ \rho(1-5|\mathbf{u}|^2)\\ \rho u_x\\ -\frac{7}{3}\rho u_x\\ \rho u_y\\ -\frac{7}{3}\rho u_y\\ \rho u_z\\ -\frac{7}{3}\rho u_z\\ \rho(2u_x^2-u_y^2-u_z^2)\\ \rho(u_y^2-u_z^2)\\ \rho u_xu_y\\ \rho u_yu_z\\ \rho u_xu_z\\ 0\end{bmatrix}+\partial_{x_1}\begin{bmatrix}\rho u_x\\ -\frac{1}{3}\rho u_x\\ -\frac{7}{3}\rho u_x\\ p+\rho u_x^2\\ \frac{1}{9}\rho B_x\\ \rho u_xu_y\\ \rho u_xu_y\\ \rho u_xu_z\\ \rho u_xu_z\\ \frac{4}{3}\rho u_x\\ 0\\ \frac{1}{3}\rho u_y\\ 0\\ \frac{1}{3}\rho u_z\\ \rho u_yu_z\end{bmatrix}+\partial_{y_1}\begin{bmatrix}\rho u_y\\ -\frac{1}{3}\rho u_y\\ -\frac{7}{3}\rho u_y\\ \rho u_xu_y\\ \rho u_xu_y\\ p+\rho u_y^2\\ \frac{1}{9}\rho B_y\\ \rho u_yu_z\\ \rho u_yu_z\\ -\frac{2}{3}\rho u_y\\ \frac{2}{3}\rho u_y\\ \frac{1}{3}\rho u_x\\ \frac{1}{3}\rho u_z\\ 0\\ \rho u_xu_z\end{bmatrix}+\partial_{z_1}\begin{bmatrix}\rho u_z\\ -\frac{1}{3}\rho u_z\\ -\frac{7}{3}\rho u_z\\ \rho u_xu_z\\ \rho u_xu_z\\ \rho u_yu_z\\ \rho u_yu_z\\ p+\rho u_z^2\\ \frac{1}{9}\rho B_z\\ -\frac{2}{3}\rho u_z\\ -\frac{2}{3}\rho u_z\\ 0\\ \frac{1}{3}\rho u_y\\ \frac{1}{3}\rho u_x\\ \rho u_xu_y\end{bmatrix}=\begin{bmatrix}0\\ -s_e'e^{(1)}\\ -s_\epsilon'\epsilon^{(1)}\\ \frac{\delta_t}{2}s_j'F_{x_1}\\ -s_q'q_x^{(1)}\\ \frac{\delta_t}{2}s_j'F_{y_1}\\ -s_q'q_y^{(1)}\\ \frac{\delta_t}{2}s_j'F_{z_1}\\ -s_q'q_z^{(1)}\\ -s_v'3p_{xx}^{(1)}\\ -s_v'p_{ww}^{(1)}\\ -s_v'p_{xy}^{(1)}\\ -s_v'p_{yz}^{(1)}\\ -s_v'p_{xz}^{(1)}\\ -s_{xyz}'m_{xzy}^{(1)}\end{bmatrix}\\ &+\begin{bmatrix}0\\ (1-\frac{s_e}{2})\left(2\mathbf{u}\cdot\mathbf{F}_1+\frac{6\sigma|\mathbf{F}_1|^2}{\psi^2(s_e^{-1}-0.5)\delta_t}\right)\\ (1-\frac{s_\epsilon}{2})(-10\mathbf{u}\cdot\mathbf{F}_1)\\ (1-\frac{s_j}{2})F_{x_1}\\ -\frac{7}{3}(1-\frac{s_q}{2})F_{x_1}\\ (1-\frac{s_j}{2})F_{y_1}\\ -\frac{7}{3}(1-\frac{s_q}{2})F_{y_1}\\ (1-\frac{s_j}{2})F_{z_1}\\ -\frac{7}{3}(1-\frac{s_q}{2})F_{z_1}\\ (1-\frac{s_v}{2})(4u_xF_{x_1}-2u_yF_{y_1}-2u_zF_{z_1})\\ (1-\frac{s_v}{2})(2u_yF_{y_1}-2u_zF_{z_1})\\ (1-\frac{s_v}{2})(u_xF_{y_1}+u_yF_{x_1})\\ (1-\frac{s_v}{2})(u_yF_{z_1}+u_zF_{y_1})\\ (1-\frac{s_v}{2})(u_xF_{z_1}+u_zF_{x_1})\\ 0\end{bmatrix}+\begin{bmatrix}0\\ \frac{4}{5}s_e'(Q_{xx_1}+Q_{yy_1}+Q_{zz_1})\\ 0\\ 0\\ 0\\ 0\\ 0\\ 0\\ 0\\ -s_v'(2Q_{xx_1}-Q_{yy_1}-Q_{zz_1})\\ -s_v'(Q_{yy_1}-Q_{zz_1})\\ -s_v'Q_{xy_1}\\ -s_v'Q_{yz_1}\\ -s_v'Q_{xz_1}\\ 0\end{bmatrix}\end{aligned} \tag{17}$$

where $p=\rho c_s^2$, $B_x=-7-21u_x^2+15u_y^2+15u_z^2$, $B_y=-7+15u_x^2-21u_y^2+15u_z^2$, $B_z=-7+15u_x^2+15u_y^2-21u_z^2$. Similarly, we can also derive the second-order hydrodynamic equations in ϵ, but we

present only the ones corresponding to the conservative variables ρ and $\rho\mathbf{u}$.

$$\partial_{t_2}\rho = 0 \tag{18a}$$

$$\begin{aligned}
&\partial_{t_2}(\rho u_x) - \frac{\delta_t}{2}\partial_{t_1}\left[(1-\frac{s_j}{2})F_{x_1}\right] + \partial_{x_1}\left[(1-\frac{s_e}{2})\frac{1}{3}e^{(1)} + (1-\frac{s_v}{2})p_{xx}^{(1)}\right] \\
&+\partial_{y_1}\left[(1-\frac{s_v}{2})p_{xy}^{(1)}\right] + \partial_{z_1}\left[(1-\frac{s_v}{2})p_{xz}^{(1)}\right] + \frac{\delta_t}{2}\partial_{t_1}\left[(1-\frac{s_j}{2})F_{x_1}\right] \\
&+\frac{\delta_t}{2}\partial_{x_1}\left[\frac{2}{3}(1-\frac{s_e}{2})(F_x u_x + F_y u_y + F_z u_z)\right. \\
&\left.+\frac{2}{3}(1-\frac{s_v}{2})(2F_x u_x - F_y u_y - F_z u_z) + \frac{1}{3}(1-\frac{s_e}{2})\frac{6\sigma(F_{x_1}^2 + F_{y_1}^2 + F_{z_1}^2)}{\psi^2(s_e^{-1}-0.5)\delta_t}\right] \\
&+\frac{\delta_t}{2}\partial_{y_1}\left[(1-\frac{s_v}{2})(F_{y_1}u_x + F_{x_1}u_y)\right] + \frac{\delta_t}{2}\partial_{z_1}\left[(1-\frac{s_v}{2})(F_{z_1}u_x + F_{x_1}u_z)\right] \\
&+\frac{\delta_t}{2}\partial_{x_1}[\frac{4}{15}s_e'(Q_{xx_1} + Q_{yy_1} + Q_{zz_1}) - \frac{1}{3}(2Q_{xx_1} - Q_{yy_1} - Q_{zz_1})s_v'] \\
&+\frac{\delta_t}{2}\partial_{y_1}(-Q_{xy_1}s_v') + \frac{\delta_t}{2}\partial_{z_1}(-Q_{xz_1}s_v') = 0
\end{aligned} \tag{18b}$$

$$\begin{aligned}
&\partial_{t_2}(\rho u_y) - \frac{\delta_t}{2}\partial_{t_1}\left[(1-\frac{s_j}{2})F_{y_1}\right] + \partial_{x_1}\left[(1-\frac{s_v}{2})p_{xy}^{(1)}\right] \\
&+\partial_{y_1}\left[(1-\frac{s_e}{2})\frac{1}{3}e^{(1)} + (1-\frac{s_v}{2})\frac{1}{2}p_{ww}^{(1)} - (1-\frac{s_v}{2})\frac{1}{2}p_{xx}^{(1)}\right] \\
&+\partial_{z_1}\left[(1-\frac{s_v}{2})p_{yz}^{(1)}\right] + \frac{\delta_t}{2}\partial_{t_1}\left[(1-\frac{s_j}{2})F_{y_1}\right] \\
&+\frac{\delta_t}{2}\partial_{x_1}\left[(1-\frac{s_v}{2})(F_{y_1}u_x + F_{x_1}u_y)\right] \\
&+\frac{\delta_t}{2}\partial_{y_1}\left[(1-\frac{s_v}{2})\frac{2}{3}(-F_{x_1}u_x + 2F_{y_1}u_y - F_{z_1}u_z)\right. \\
&\left.+\frac{2}{3}(1-\frac{s_e}{2})(F_{x_1}u_x + F_{y_1}u_y + F_{z_1}u_z) + \frac{1}{3}(1-\frac{s_e}{2})\frac{6\sigma(F_{x_1}^2 + F_{y_1}^2 + F_{z_1}^2)}{\psi^2(s_e^{-1}-0.5)\delta_t}\right] \\
&+\frac{\delta_t}{2}\partial_{z_1}\left[(1-\frac{s_v}{2})p_{yz}^{(1)}\right] + \frac{\delta_t}{2}\partial_{x_1}(-Q_{xy_1}s_v') \\
&+\frac{\delta_t}{2}\partial_{y_1}[\frac{4}{15}s_e'(Q_{xx_1} + Q_{yy_1} + Q_{zz_1}) + \frac{s_v'}{3}(Q_{xx_1} - 2Q_{yy_1} + Q_{zz_1})] \\
&+\frac{\delta_t}{2}\partial_{z_1}(-Q_{yz_1}s_v') = 0
\end{aligned} \tag{18c}$$

$$\begin{aligned}
&\partial_{t_2}(\rho u_z) - \frac{\delta_t}{2}\partial_{t_1}\left[(1-\frac{s_j}{2})F_{z_1}\right] + \partial_{x_1}\left[(1-\frac{s_v}{2})p_{xz}^{(1)}\right] + \partial_{y_1}\left[(1-\frac{s_v}{2})p_{yz}^{(1)}\right] \\
&+\partial_{z_1}\left[(1-\frac{s_e}{2})\frac{1}{3}e^{(1)} - (1-\frac{s_v}{2})\frac{1}{2}p_{ww}^{(1)} - (1-\frac{s_v}{2})\frac{1}{2}p_{xx}^{(1)}\right] \\
&+\frac{\delta_t}{2}\left[\partial_{t_1}(1-\frac{s_j}{2})F_{z_1}\right] + \frac{\delta_t}{2}\partial_{x_1}\left[(1-\frac{s_v}{2})(F_{z_1}u_x + F_{x_1}u_z)\right] \\
&+\frac{\delta_t}{2}\partial_{y_1}\left[(1-\frac{s_v}{2})(F_{z_1}u_y + F_{y_1}u_z)\right] \\
&+\frac{\delta_t}{2}\partial_{z_1}\left[(1-\frac{s_e}{2})\frac{2}{3}(F_{x_1}u_x + F_{y_1}u_y + F_{z_1}u_z)\right. \\
&\left.-\frac{2}{3}(1-\frac{s_v}{2})(F_{x_1}u_x + F_{y_1}u_y - 2F_{z_1}u_z) + \frac{1}{3}(1-\frac{s_e}{2})\frac{6\sigma(F_{x_1}^2 + F_{y_1}^2 + F_{z_1}^2)}{\psi^2(s_e^{-1}-0.5)\delta_t}\right] \\
&+\frac{\delta_t}{2}\partial_{x_1}(-Q_{xz_1}s_v') + \frac{\delta_t}{2}\partial_{y_1}(-Q_{yz_1}s_v') \\
&+\frac{\delta_t}{2}\partial_{z_1}\left[\frac{4}{15}s_e'(Q_{xx_1} + Q_{yy_1} + Q_{zz_1}) + \frac{s_v'}{3}(Q_{xx_1} + Q_{yy_1} - 2Q_{zz_1})\right] = 0
\end{aligned} \tag{18d}$$

Neglecting the term $O(|\mathbf{u}|^3)$ and with the aid of Eq. (17), we obtain the following equations for $e^{(1)}$, $p_{xx}^{(1)}$, $p_{ww}^{(1)}$, $p_{xy}^{(1)}$, $p_{yz}^{(1)}$ and $p_{xz}^{(1)}$:

$$\begin{aligned}
-s_e'e^{(1)} &= 2p(\partial_{x_1}u_x + \partial_{y_1}u_y + \partial_{z_1}u_z) + s_e(u_xF_{x_1} + u_yF_{y_1} + u_zF_{z_1}) \\
&\quad - \frac{6\sigma(F_{x_1}^2 + F_{y_1}^2 + F_{z_1}^2)s_e}{\psi^2\delta_t} - \frac{4}{5}s_e'(Q_{xx_1} + Q_{yy_1} + Q_{zz_1})
\end{aligned} \tag{19a}$$

$$\begin{aligned}
-s_v'3p_{xx}^{(1)} &= 2p(2\partial_{x_1}u_x - \partial_{y_1}u_y - \partial_{z_1}u_z) + s_v(2u_xF_{x_1} - u_yF_{y_1} \\
&\quad - u_zF_{z_1}) + s_v'(2Q_{xx_1} - Q_{yy_1} - Q_{zz_1})
\end{aligned} \tag{19b}$$

$$-s_v'p_{ww}^{(1)} = 2p(\partial_{y_1}u_y - \partial_{z_1}u_z) + s_v(u_yF_{y_1} - u_zF_{z_1}) + s_v'(Q_{yy_1} - Q_{zz_1}) \tag{19c}$$

$$-s_v'p_{xy}^{(1)} = p(\partial_{x_1}u_y + \partial_{y_1}u_x) + \frac{s_v}{2}(u_xF_{y_1} + u_yF_{x_1}) + s_v'Q_{xy_1} \tag{19d}$$

$$-s_v'p_{yz}^{(1)} = p(\partial_{y_1}u_z + \partial_{z_1}u_y) + \frac{s_v}{2}(u_yF_{z_1} + u_zF_{y_1}) + s_v'Q_{yz_1} \tag{19e}$$

$$-s_v'p_{xz}^{(1)} = p(\partial_{x_1}u_z + \partial_{z_1}u_x) + \frac{s_v}{2}(u_xF_{z_1} + u_zF_{x_1}) + s_v'Q_{xz_1} \tag{19f}$$

Substituting Eq. (19) into Eq. (18) results in the second-order hydrodynamic equations in ϵ as

$$\partial_{t_2}\rho = 0 \tag{20a}$$

$$\begin{aligned}
\partial_{t_2}(\rho u_x) &= \partial_{x_1}\left[\rho\xi(\partial_{x_1}u_x + \partial_{y_1}u_y + \partial_{z_1}u_z)\right. \\
&\quad + \frac{2}{3}\rho\nu(2\partial_{x_1}u_x - \partial_{y_1}u_y - \partial_{z_1}u_z) - \frac{2\sigma(F_{x_1}^2 + F_{y_1}^2 + F_{z_1}^2)}{\psi^2} \\
&\quad \left.+(\frac{2}{5}Q_{xx_1} - \frac{3}{5}Q_{yy_1} - \frac{3}{5}Q_{zz_1})\right] \\
&\quad + \partial_{y_1}\left[\rho\nu(\partial_{x_1}u_y + \partial_{y_1}u_x) + Q_{xy_1}\right] \\
&\quad + \partial_{z_1}\left[\rho\nu(\partial_{x_1}u_z + \partial_{z_1}u_x) + Q_{xz_1}\right]
\end{aligned} \tag{20b}$$

$$\begin{aligned}
\partial_{t_2}(\rho u_y) &= \partial_{x_1}\left[\rho\nu(\partial_{x_1}u_y + \partial_{y_1}u_x) + Q_{xy_1}\right] \\
&\quad + \partial_{y_1}\left[\rho\xi(\partial_{x_1}u_x + \partial_{y_1}u_y + \partial_{z_1}u_z)\right. \\
&\quad + \frac{2}{3}\rho\nu(-\partial_{x_1}u_x + 2\partial_{y_1}u_y - \partial_{z_1}u_z) - \frac{2\sigma(F_{x_1}^2 + F_{y_1}^2 + F_{z_1}^2)}{\psi^2} \\
&\quad \left.+(-\frac{3}{5}Q_{xx_1} + \frac{2}{5}Q_{yy_1} - \frac{3}{5}Q_{zz_1})\right] \\
&\quad + \partial_{z_1}\left[\rho\nu(\partial_{y_1}u_z + \partial_{z_1}u_y) + Q_{xz_1}\right]
\end{aligned} \tag{20c}$$

$$\begin{aligned}
\partial_{t_2}(\rho u_z) &= \partial_{x_1}\left[\rho\nu(\partial_{x_1}u_z + \partial_{z_1}u_x) + Q_{xz_1}\right] \\
&\quad + \partial_{y_1}\left[\rho\nu(\partial_{y_1}u_z + \partial_{z_1}u_y) + Q_{yz_1}\right] \\
&\quad + \partial_{z_1}\left[\rho\xi(\partial_{x_1}u_x + \partial_{y_1}u_y + \partial_{z_1}u_z)\right. \\
&\quad - \frac{2}{3}\rho\nu(\partial_{x_1}u_x + \partial_{y_1}u_y - 2\partial_{z_1}u_z) \\
&\quad \left.- \frac{2\sigma(F_{x_1}^2 + F_{y_1}^2 + F_{z_1}^2)}{\psi^2} + (-\frac{3}{5}Q_{xx_1} - \frac{3}{5}Q_{yy_1} + \frac{2}{5}Q_{zz_1})\right]
\end{aligned} \tag{20d}$$

where ν and ξ are the kinematic and bulk viscosities and given by

$$\nu = \frac{1}{3}\left(\frac{1}{s_v} - \frac{1}{2}\right)\delta_t, \quad \xi = \frac{2}{9}\left(\frac{1}{s_e} - \frac{1}{2}\right)\delta_t \tag{21}$$

Applying the Taylor expansion to Eqs. (8) and (11) yields

$$\mathbf{F} = -Gc^2\left[\psi\nabla\psi + \frac{1}{6}c^2\psi\nabla(\nabla^2\psi) + \ldots\right] \tag{22a}$$

$$\mathbf{Q} = \frac{1}{12}\kappa Gc^4\left[\psi\nabla^2\psi\mathbf{I} + 2\psi\nabla\nabla\psi + \ldots\right] \tag{22b}$$

Combining the results at the t_1 and t_2 time scales, i.e., Eqs. (17) and (20), and with the aid of Eq. (22), we obtain the following macroscopic equations:

$$\frac{\partial\rho}{\partial t} + \nabla\cdot(\rho\mathbf{u}) = 0 \tag{23a}$$

$$\begin{aligned}
\frac{\partial(\rho\mathbf{u})}{\partial t} + \nabla\cdot(\rho\mathbf{u}\mathbf{u}) &= -\nabla\cdot(\rho c_s^2\mathbf{I}) + \nabla\cdot\mathbf{\Pi} + \mathbf{F} - 2G^2c^4\sigma\nabla\cdot(|\nabla\psi|^2\mathbf{I}) \\
&\quad - \nabla\cdot\left[\kappa\frac{Gc^4}{6}(\psi\nabla^2\psi\mathbf{I} - \psi\nabla\nabla\psi)\right]
\end{aligned} \tag{23b}$$

where $\mathbf{\Pi}$ is shear stress and defined by

$$\mathbf{\Pi} = \rho\nu\left[\nabla\mathbf{u} + (\nabla\mathbf{u})^T\right] + \rho\left(\xi - \frac{2}{3}\nu\right)(\nabla\cdot\mathbf{u})\mathbf{I} \tag{24}$$

Define the discrete form pressure tensor $\mathbf{P}$ as (Shan, 2008)

$$\sum \mathbf{P}\cdot\mathbf{A} = \sum \rho c_s^2 \mathbf{I}\cdot\mathbf{A} - \sum \mathbf{F} \tag{25}$$

where $\mathbf{A}$ is an area element. Combines Eqs. (25) and (23b), then the discrete form pressure tensor will be given by

$$\mathbf{P} = \left[\rho c_s^2 + \frac{Gc^2}{2}\psi^2 + \frac{Gc^4}{12}(1+2\kappa)\psi\nabla^2\psi + 2\sigma G^2 c^4|\nabla\psi|^2\right]\times\mathbf{I} + \frac{Gc^4}{6}(1-\kappa)\psi\nabla\nabla\psi \tag{26}$$

where c_s^2 denotes the speed of the sound and $c_s^2 = 1/3c^2$ for D3Q15 model. Following Shan's work (Shan, 2008), the surface tension coefficient is defined as

$$\gamma = \int_{-\infty}^{\infty}(p_0 - p_T)dz = -\frac{Gc^4(1-\kappa)}{6}\int_{\rho_g}^{\rho_l}\psi I^2\left(\frac{d\rho}{dz}\right)d\rho \tag{27}$$

where p_n is the normal pressure tensor, p_T is the transversal pressure tensor, and $\psi' = d\psi/d\rho$. Here, we take the z direction as the normal direction of the flat interface. When $\sigma = 0$ and $\kappa = 0$, Eq. (26) will reduce to the standard pressure tensor of the pseudopotential LB model. The mechanical stability condition (Li and Luo, 2013) is given as $\epsilon = -2(\alpha + 24G\sigma)/\beta$, where α and β are given by Shan (2008) $\alpha = 0$ and $\beta = 3$, respectively. It has been shown in Li et al. (2012) that the parameter ϵ is chosen as $1 < \epsilon < 2$ to make the mechanical stability condition approximate the thermodynamic consistency requirement. In the present study, we fix $G = -1$, thus the parameter σ is calculated as $0.0625 < \sigma < 0.125$. The exact value of parameter σ is further determined by fitting the Maxwell construction solution as illustrated in the following section.

3. Simulation results and discussion

3.1. Evaluation of thermodynamic consistency

We consider a flat interface problem to compare the coexistence curves obtained numerically and given by Maxwell construction. Two equations of state for non-ideal gases are considered (Yuan and Schaefer, 2006):

1. The Carnahan–Starling (C–S) equation of state is given by

$$p_{EOS} = \rho RT\frac{1 + b\rho/4 + (b\rho/4)^2 - (b\rho/4)^3}{(1-b\rho/4)^3} - a\rho^2 \tag{28}$$

where $a = 0.4963R^2T_c^2/p_c$, $b = 0.18727RT_c/p_c$, T is temperature and subscript of c denotes the critical value. Setting $a = 0.25$, $R = 1$, and $R = 1$, then T_c would be given by 0.02358.

2. The Peng–Robinson (P–R) equation of state is given by

$$p_{EOS} = \frac{\rho RT}{1-b\rho} - \frac{a\alpha(T)\rho^2}{1 + 2b\rho - b^2\rho^2} \tag{29}$$

where $\alpha(T) = \left[1 + (0.37464 + 1.54226\omega - 0.26992\omega^2)\times(1 - \sqrt{T/T_c})\right]^2$, with ω being the acentric factor determined by the substance under consideration. Here, we choose $\omega = 0.344$, which is the acentric factor of water. The critical properties are given by $a = 0.45724R^2T_c^2/p_c$ and $b = 0.0778RT_c/p_c$. Setting $a = 1/100$, $b = 2/21$, and $R = 1$, T_c would be given by 0.017866.

In the simulations, the interaction strength G in Eq. (8) is fixed as $G = -1$, and the interaction potential $\psi(\mathbf{x})$ is determined as $\psi(\mathbf{x}) = \sqrt{2(p_{EOS} - \rho c_s^2)/Gc^2}$. A $100\times100\times100$ lattice is adopted. The periodical boundary conditions are applied in all three directions, and the density field is initialized as follows:

$$\rho(x,y,z) = \rho_g + \frac{\rho_l - \rho_g}{2}[\tanh(z_1) - \tanh(z_2)] \tag{30}$$

where $z_1 = 2(z-25)/W$, $z_2 = 2(z-75)/W$ and $W = 5$ is the initial interface thickness. The parameter κ in Eq. (11) is set to be $\kappa = 0$.

The coexistence curves obtained from $\sigma = 0.12$ are shown in Fig. 1. It clearly demonstrates that the present forcing scheme is capable of achieving thermodynamic consistency and large density ratio in the MRT pseudo-potential LB model.

3.2. Evaluation of Laplace's law

The validation of the model with Laplace's law is made by simulating droplets with different radii. According to Laplace's law, the pressure difference across a circular interface is related to the surface tension γ and the droplet radius R via $\delta p = p_{in} - p_{out} = 2\gamma/R$. When the surface tension is given, the pressure difference δp will be proportional to $1/R$.

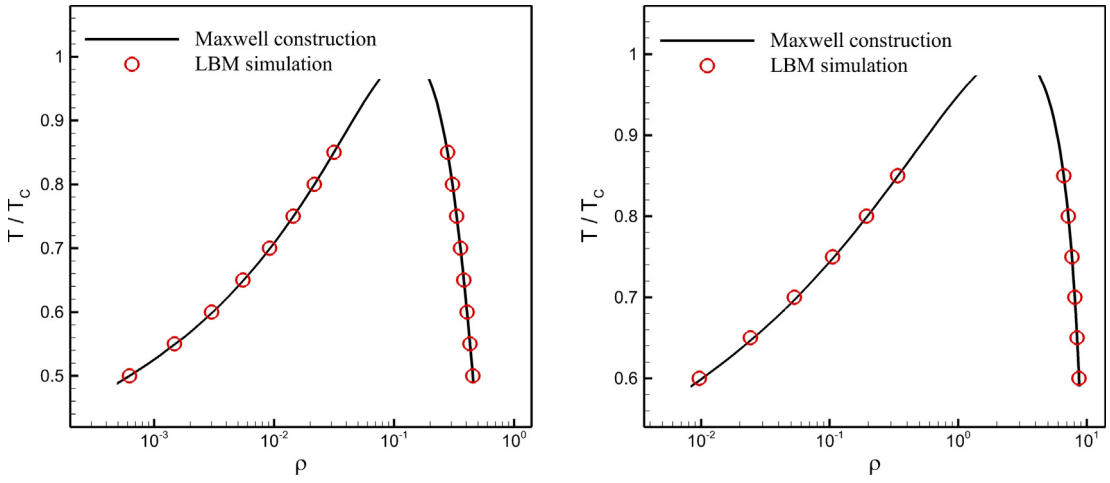

(a) Coexistence curve of the C-S EOS (b) Coexistence curve of the P-R EOS

Fig. 1. Comparison of the numerical coexistence curves with the coexistence curves given by Maxwell construction.

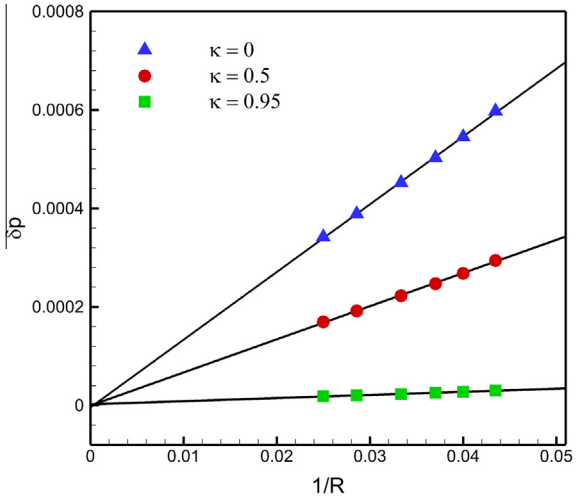

Fig. 2. Numerical validation of the Laplace's law.

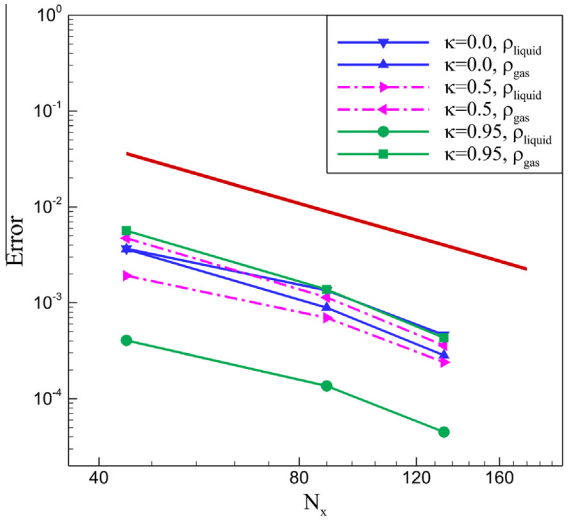

Fig. 3. Errors of the densities of liquid and gas as a function of mesh size.

Table 1
Comparison of spurious velocities $|\mathbf{u}^s|_{\max}$ in SRT and MRT simulations.

		$\kappa = 0$	$\kappa = 0.5$	$\kappa = 0.95$
$s_v^{-1} = 0.6$	SRT	NaN	NaN	NaN
	MRT	0.05571	0.05662	0.06745
$s_v^{-1} = 1.0$	SRT	0.04068	0.03490	0.02792
	MRT	0.03201	0.02682	0.02133

In the simulations, a $120 \times 120 \times 120$ lattice is adopted. The periodical boundary conditions are applied in all three directions, and the density field is initialized as

$$\rho(x,y,z) = \frac{\rho_l + \rho_g}{2} + \frac{\rho_l - \rho_g}{2} \times \left[\tanh\left(\frac{2(\sqrt{(x-x_0)^2 + (y-y_0)^2 + (z-z_0)^2} - R)}{W}\right)\right] \quad (31)$$

where (x_0, y_0, z_0) is the center position of the computational domain, R is the radius of the droplet, and $W = 5$ is the initial interface width. C–S EOS is used and the parameter σ in Eq. (10) is set to be $\sigma = 0.12$ to achieve thermodynamic consistency. The temperature is $T = 0.5T_c$, which corresponds to $\rho_l/\rho_g \approx 720$. The numerical pressure differences at $\kappa = 0,\ 0.5,\ 0.95$ with $20 < R < 40$ are shown in Fig. 2. The solid lines denote linear fit of the LB simulation results. The coefficients of determination are 0.9998, 0.9994, 0.9978, respectively, which means the pressure difference inside and outside the droplet is indeed proportional to the reciprocal of the radius, and Laplace's law is well satisfied.

3.3. Evaluation of spurious velocities

The spurious velocities in the simulations are investigated in order to compare the performance of the proposed MRT model with single-relaxation-time (SRT) model. The MRT model relaxes various moments (e.g., density, energy, momentum, heat flux, stress tensor) to their equilibrium states at different relaxation times during collisions, and reduces to the SRT model once the parameters of the relaxation matrix s_i in $\mathbf{S} = \mathrm{diag}(s_\rho, s_e, s_\epsilon, s_j, s_q, s_j, s_q, s_j, s_q, s_v, s_v, s_v, s_v, s_v, s_{xyz})$ are equal to each other. In the simulations, a $120 \times 120 \times 120$ lattice is adopted, and the radius of the droplet is set to be $R = 30$. The boundary conditions are periodical in all three directions, and density field are initialized using Eq. (31). In the SRT model, the relaxation times are choose as $s_\rho = s_e = s_\epsilon = s_j = s_q = s_{xyz} = s_v$; while in the MRT model, $s_\rho = 1.0$, $s_e = 1.1$, $s_\epsilon = 1.1$, $s_j = 1.0$, $s_q = 1.1$, and $s_{xyz} = 1.2$. Table 1 compares the maximum spurious velocities at the density ratio of $\rho_l/\rho_g \approx 720$. We can see that the use of MRT model reduces the spurious velocities and enhances the numerical stability.

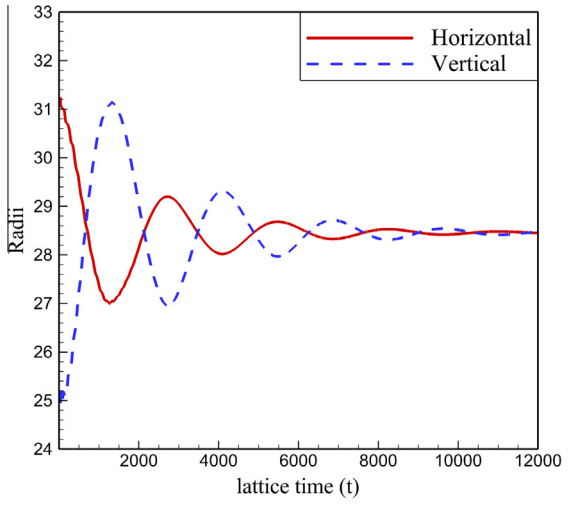

Fig. 4. Radii of the oscillatory spheroid as a function of time.

3.4. Evaluation of spatial accuracy

The spatial accuracy of the present model is tested by the case of a spherical droplet. In the simulations, different mesh sizes $N_x \times N_y \times N_z = 44 \times 44 \times 44$, $88 \times 88 \times 88$, $132 \times 132 \times 132$, and $176 \times 176 \times 176$ are used. The radius of the droplet is $R = N_x/4$. The boundary conditions are periodical in all three directions, and density field are initialized using Eq. (31). We assume the mesh $176 \times 176 \times 176$ is the finest mesh and the result at this mesh is accurate. The error of mesh size N_x is defined as $\mathrm{Error}(N_x) = |\rho(N_x) - \rho(176)|$, where $\rho(N_x)$ stands for the density of liquid or gas obtained by mesh size $N_x \times N_x \times N_x$. The errors are illustrated in Fig. 3, where the top thick red line represents exact second-order spatial accuracy, so we can see the present model is approximately second-order accuracy in space.

3.5. Evaluation of droplet oscillation

In addition to steady-sate problems, the present model is also validated by dynamic case. Here, we simulate the droplet oscillation. The frequency for the nth mode of droplet oscillation is given by Miller and Scriven (1968)

$$\omega_n = \omega_n^* - \frac{1}{2}\alpha\omega_n^{*\frac{1}{2}} + \frac{1}{4}\alpha^2 \tag{32}$$

where ω_n is the angular response frequency and ω_n^* is Lamb's natural resonance frequency (Lamb, 1932)

$$(\omega_n^*)^2 = \frac{n(n+1)(n-1)(n+2)}{R_d^3\left[n\rho_g + (n+1)\rho_l\right]}\gamma \tag{33}$$

where R_d is the equilibrium radius of the drop, and γ is the interfacial surface tension. The parameter α is given by Miller and Scriven (1968)

$$\alpha = \frac{(2n+1)^2(\mu_l\mu_g\rho_l\rho_g)^{1/2}}{\sqrt{2}R_d[n\rho_g + (n+1)\rho_l][(\mu_l\rho_l)^{1/2} + (\mu_g\rho_g)^{1/2}]} \tag{34}$$

where μ_l and μ_g are the dynamic viscosity of the liquid and gas, respectively.

In the simulations, an ellipsoidal drop is used for the initial condition

$$\frac{(x-x_0)^2}{R^2} + \frac{(y-y_0)^2}{R^2} + \frac{(z-z_0)^2}{(0.8R)^2} = 1 \tag{35}$$

where (x_0, y_0, z_0) is the center of the ellipsoid and the computational domain. The radius is set to be $R = 30$ and the ellipsoid is initially placed in the center of the computational domain. Fig. 4 shows the radii of the spheroid as a function of lattice time. The solid line and the dashed line represent the radius measured from the center of the droplet in horizontal and vertical directions, respectively. When the solid line and the dashed line cross, the drop is spherical. Due to the viscous dissipation, the amplitude of the oscillation decreases with time. The theoretical prediction of the time period calculated from the second mode ($n = 2$) of oscillation is $T_{\text{anal}} = 2601$, while the result given by the present LB model is $T_{\text{LBM}} = 2701$, with relative error 6.5%.

3.6. Evaluation of contact angle

Fig. 5 demonstrates that different contact angles can be obtained through adjusting the parameter G_{ads} in Eq. (12). In these simulations, no body force $\mathbf{F}_{\text{body}}$ is applied, and a semi-sphere stationary droplet with a radius of $r = 25$ is initially placed on a flat homogeneous solid surface. The computational domain size is $120 \times 120 \times 80$ lattice; the upper and lower boundaries are solid walls; and the periodical boundary conditions are employed in the X and Y directions. C–S EOS is used and the temperature is $T = 0.5T_c$, which corresponds to $\rho_l/\rho_g \approx 720$.

3.7. Droplets motion in a microchannel

Understanding the droplet dynamics on the solid phase is of great importance to many microfluidic devices (Kang et al., 2005; Hao and Cheng, 2009; Gong and Cheng, 2012; Liu et al., 2014). For example, water management is considered to be a critical issue on the performance of proton exchange membrane fuel cells (PEMFC). In a PEMFC cathode, air is supplied to the gas channel and transport to the catalyst layer where electrochemical reactions occur and water is produced. In order to maintain high proton conductivity of the membrane, it is necessary to keep sufficient water. On the other hand, however, too much water can cause clogging of the gas channel, hindering transportation of gas to the reaction sites, and leading to serious degradation of fuel cell performance. The application of the LB multiphase model to study water droplet dynamics in a microchannel will provide a basic understanding for the droplet behavior in a PEMFC gas channel.

In the following, we apply the three-dimensional LB multiphase model to investigate the effects of droplet surface tension, channel surface wettability, and channel surface roughness on the motion of droplets in a microchannel. In the simulations, the body force $\mathbf{F}_{\text{body}}$ in Eq. (13) is calculated as $\mathbf{F}_{\text{body}} = \mathbf{g}(\rho - \rho_g)$, which means that the body force only affects the liquid phase. For simplicity, we choose $\mathbf{g} = (g, 0, 0)$, and g is fixed as $g = 5 \times 10^{-6}$. The

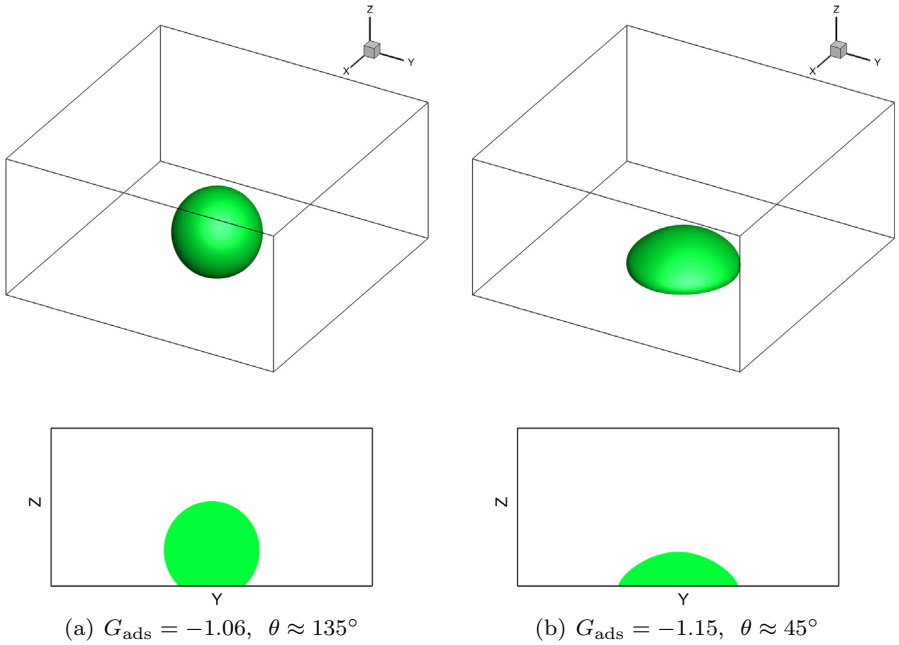

(a) $G_{\text{ads}} = -1.06,\ \theta \approx 135°$ (b) $G_{\text{ads}} = -1.15,\ \theta \approx 45°$

Fig. 5. Different contact angles obtained through adjusting the parameter G_{ads}. The lower 2D figures are the cross-sectional view on the middle section along the Y direction.

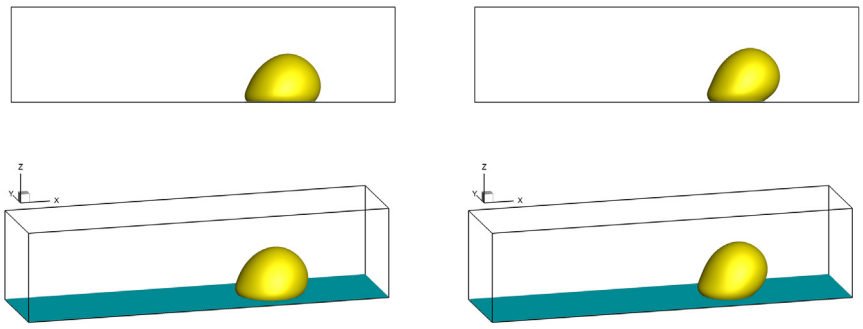

(a) $\kappa = 0.25$ (b) $\kappa = 0.5$

Fig. 6. The droplets shape with different surface tension. The upper 2D figures are the cross-sectional view on the middle section along the channel.

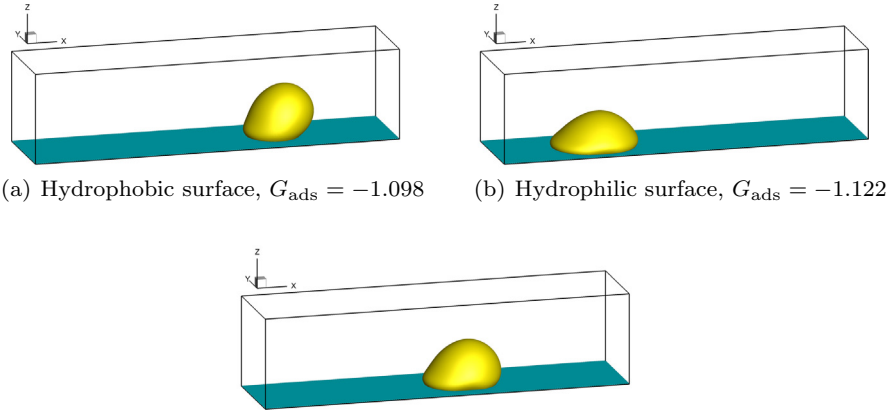

(a) Hydrophobic surface, $G_{\text{ads}} = -1.098$ (b) Hydrophilic surface, $G_{\text{ads}} = -1.122$

(c) Mixed wettability surface, G_{ads} change linearly from -1.098 to -1.122

Fig. 7. The droplet shape and its position at $t = 50,000$.

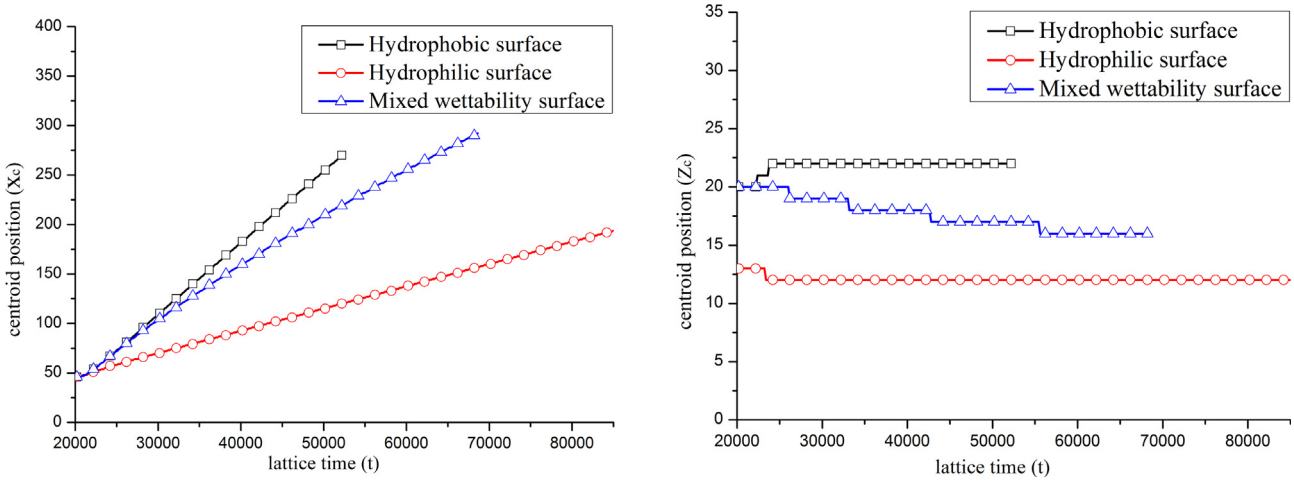

(a) Droplet centroid (x_c) position in horizontal direction (b) Droplet centroid (z_c) position in vertical direction

Fig. 8. The motion of droplet centroid position in three different microchannels.

computational domain is taken as $N_x \times N_y \times N_z = 361 \times 91 \times 91$ and a liquid droplet having a radius of $R = 34$ with its center at $(91, 46, 17)$ is initially placed in contact with the bottom surface. C–S EOS is used and the parameter σ in Eq. (10) is set to be $\sigma = 0.12$ to achieve thermodynamic consistency. The temperature is $T = 0.52T_c$, which corresponds to $\rho_l \approx 0.4444$, $\rho_g \approx 0.0009$ and $\rho_l/\rho_g \approx 490$. Periodic boundary condition is applied in the X direction, while non-slip bounce back boundary condition is applied on the four walls ($Y = 1$, $Y = 91$, $Z = 1$, and $Z = 91$).

3.7.1. Effects of droplet surface tension

A feature of the present pseudo-potential based LB multiphase model is that surface tension is a variable independent of density ratio. To demonstrate this feature, droplets with different values

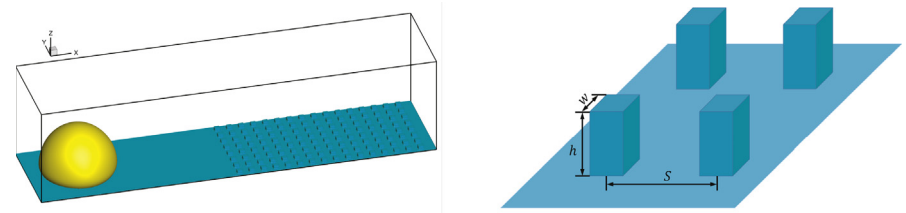

(a) 3D view of microchannel with roughness (b) Schematic drawing of microstructure of rough channel surface

Fig. 9. Geometries for the microchannel with roughness.

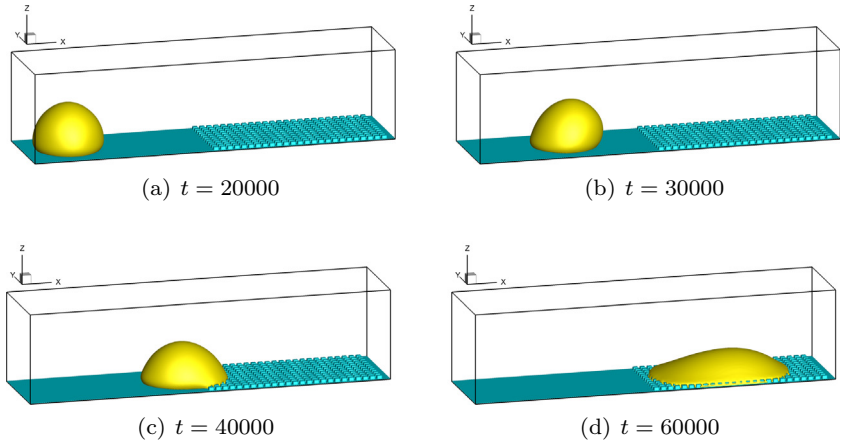

(a) $t = 20000$ (b) $t = 30000$

(c) $t = 40000$ (d) $t = 60000$

Fig. 10. Droplet motion on the rough microchannel surface ($S = 3$).

of surface tension and the same density ratio is set initially. The surface tension γ can be varied by adjusting the parameter κ in Eq. (11), while the contact angle θ is kept the same by adjusting the parameter G_{ads} in Eq. (12). Define the capillary number (Ca) as $Ca = \mu U/\gamma$, which represents the ratio of viscous force to interfacial force, and the Bond number (Bo) as $Bo = \Delta\rho g L^2/\gamma$, which represents the ratio of gravitational force to surface force. Here, U is the terminal droplet moving velocity, L is the diameter of the droplet. The surface tension γ is determined by Laplace's law, and the dynamic viscosity μ is calculated as $\mu = \rho\nu = \rho c_s^2(s_\nu^{-1} - 0.5)$ with $s_\nu^{-1} = 0.8$. Fig. 6 compares the droplet shapes during motion along the microchannel surface. In case (a), $U = 0.009$ and $\gamma = 0.01005$, thus $Ca = 0.039$ and $Bo = 1.02$; in case (b), $U = 0.0112$ and $\gamma = 0.007835$, thus $Ca = 0.063$ and $Bo = 1.31$. With a decrease in surface tension (i.e., increasing parameter κ), the droplet deformation is found to be increased. This phenomenon implies that the droplet stretched more with a larger capillary number and Bond number. In addition, the dynamic contact angles are different as a result of various droplet surface tension.

3.7.2. Effects of channel surface wettability

Three microchannels with different surface wettabilities are considered: Case (a), uniform hydrophobic surface; Case (b), uniform hydrophilic surface; Case (c), heterogeneous surface with mixed wettabilities. In Cases (a) and (b), uniform static contact angles are adopted along the channel surfaces by setting uniform fluid–solid interaction G_{ads} along the X direction, while in Case (c), G_{ads} changes linearly from $X = 0$ to $X = 1$, thus the static contact angle gradually varies along the X direction. Initially the surface tension of these three droplets are the same, by fixing the

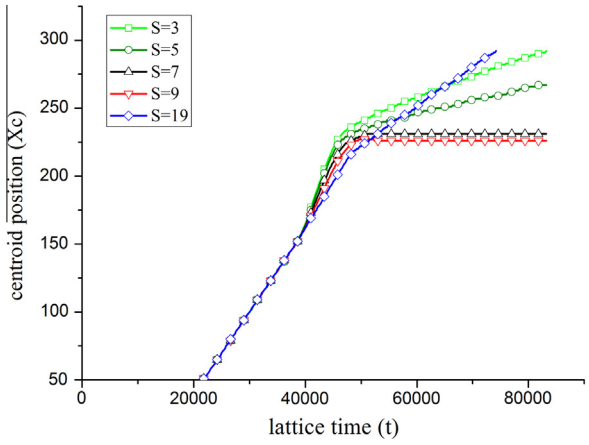

Fig. 11. Droplet motion on bottom surface with different micropillar spacings.

parameter κ in Eq. (11) as $\kappa = 0.5$. Fig. 7 shows the droplet shape and its position at $t = 50,000$.

To quantitively describe the droplet distribution along the microchannel surface and the time required for droplet removal, we define the centroid of the droplet as

$$\mathbf{X}_c = (x_c, y_c, z_c) = \frac{\int_{\Omega_l} \mathbf{x} dx}{\int_{\Omega_l} 1 dx} \tag{36}$$

where Ω_l denotes the region that the droplet occupies. The motion of droplet centroids position in these three channels is plotted in Fig. 8.

Droplets motion on a hydrophobic microchannel surface takes much shorter time than on hydrophilic surface. On the other hand,

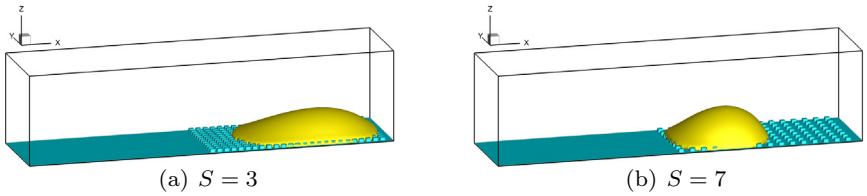

(a) $S = 3$ (b) $S = 7$

Fig. 12. Droplet shape and position on microchannel rough surface with micropillar spacing $S = 3$ and $S = 7$ at $t = 80,000$.

however, droplet clogging is more easily caused by hydrophobic microchannel, since the droplets have relative higher centroid position in vertical direction. While on a hydrophilic microchannel surface, the droplet adheres the microchannel wall, leaving some voids in the microchannel for gaseous transportation. A compromise is a heterogeneous microchannel surface with mixed wettability, i.e., wettability changes gradually from hydrophobic to hydrophilic, such characteristics could be used to enhance droplets removal and gases transport in microchannels.

3.7.3. Effects of channel surface roughness

The roughness is simplified as a group of micropillars on the lower channel wall, as illustrated in Fig. 9. The micropillar are distributed evenly in the microchannel with width w, height h and spacing S. In the simulations, we fix $w = 4$ lattice, $h = 5$ lattice, and investigate the effect of S on the droplet motion.

Fig. 10 shows snapshots of droplet motion on the bottom surface with micropillar spacing $S = 3$ lattice in a microchannel, while Fig. 11 gives the droplet centroid position (X_c) as a function of lattice time (t) for varying micropillar spacings (S). In the simulations, a stationary droplet is formed at $t = 0$ and an equilibrium state is reached at $t = 20,000$. At this equilibrium state, the droplet becomes a truncated sphere in shape as shown in Fig. 10(a). Beginning at this moment ($t = 20,000$), the external body force $\mathbf{F}_{\text{body}}$ is suddenly added, driving the droplet motion. In all simulations, the droplets move with the same velocity and same shape in the flat regions as shown in Fig. 10(b), until at $t = 39,000$ they reach the rough areas. After that, droplets motion on bottom surface with different micropillar spacing (S) show different behaviors. The droplets velocities increase at first stage (e.g., Fig. 10(c)), and then decrease at second stage (e.g., Fig. 10(d)). The increase of droplets velocities in the first stage is due to large adhesion force at the spacings, driving the droplet to adhere between the spacings; while the decrease of droplets velocities in the second stage is due to the large gaps between the micropillars, resulting in droplets falling down into the roughness. Also, at the second stage, the effect of micropillar spacing to droplet interface thickness ratio is remarkable. When the micropillar spacing S is larger than the droplet interface thickness (usually 3–5 lattice in the simulations), for example, as $S = 7$ shown in Fig. 12(b), the droplet will be trapped in the rough region and could no longer be removed out. For very large micropillar spacing, (e.g., $S = 19$), which is the limiting case of flat surface, the droplet could also be removed out.

4. Conclusion

In this work, we have presented a three-dimensional pseudopotential-based LB model with an improved forcing scheme for multiphase flows. The numerical validations demonstrate that the present model allows large density ratio (around 700 in static and quasi-static cases) and variable surface tension flows to be more realistically simulated. The application of the model to the droplet motion in a microchannel shows that the channel surface with mixed wettability enhances droplets removal and gases transport in microchannels. It is also observed that inappropriate design of micropillar spacing leads to droplets trapping, thus hindering droplets removal.

Acknowledgement

The work described in this paper was fully supported by a grant from the Research Grants Council of the Hong Kong Special Administrative Region, China (Project No. 16213414).

References

Badalassi, V., Ceniceros, H., Banerjee, S., 2003. Computation of multiphase systems with phase field models. J. Comput. Phys. 190 (2), 371–397.
Benzi, R., Biferale, L., Sbragaglia, M., Succi, S., Toschi, F., 2006. Mesoscopic modeling of a two-phase flow in the presence of boundaries: the contact angle. Phys. Rev. E 74 (2), 021509.
Chai, Z., Zhao, T., 2012. Effect of the forcing term in the multiple-relaxation-time lattice boltzmann equation on the shear stress or the strain rate tensor. Phys. Rev. E 86 (1), 016705.
Chen, S., Doolen, G.D., 1998. Lattice boltzmann method for fluid flows. Ann. Rev. Fluid Mech. 30 (1), 329–364.
Chen, L., Kang, Q., Mu, Y., He, Y.-L., Tao, W.-Q., 2014. A critical review of the pseudopotential multiphase lattice boltzmann model: methods and applications. Int. J. Heat Mass Transfer 76, 210–236.
Cheng, P., Quan, X., Gong, S., Liu, X., Yang, L., 2014. Chapter four-recent analytical and numerical studies on phase-change heat transfer. Adv. Heat Transfer 46, 187–248.
d'Humières, D., 2002. Multiple-relaxation-time lattice boltzmann models in three dimensions. Philos. Trans. Roy. Soc. Lond. Ser. A: Math. Phys. Eng. Sci. 360 (1792), 437–451.
Gong, S., Cheng, P., 2012. Numerical investigation of droplet motion and coalescence by an improved lattice boltzmann model for phase transitions and multiphase flows. Comput. Fluids 53, 93–104.
Grunau, D., Chen, S., Eggert, K., 1993. A lattice boltzmann model for multiphase fluid flows. Phys. Fluids A: Fluid Dyn. (1989–1993) 5 (10), 2557–2562.
Gunstensen, A.K., Rothman, D.H., Zaleski, S., Zanetti, G., 1991. Lattice boltzmann model of immiscible fluids. Phys. Rev. A 43 (8), 4320.
Hao, L., Cheng, P., 2009. Lattice boltzmann simulations of liquid droplet dynamic behavior on a hydrophobic surface of a gas flow channel. J. Power Sources 190 (2), 435–446.
He, X., Doolen, G.D., 2002. Thermodynamic foundations of kinetic theory and lattice boltzmann models for multiphase flows. J. Stat. Phys. 107 (1–2), 309–328.
He, X., Shan, X., Doolen, G.D., 1998. Discrete boltzmann equation model for nonideal gases. Phys. Rev. E 57 (1), R13.
Hirt, C.W., Nichols, B.D., 1981. Volume of fluid (vof) method for the dynamics of free boundaries. J. Comput. Phys. 39 (1), 201–225.
Huang, H., Krafczyk, M., Lu, X., 2011. Forcing term in single-phase and Shan–Chen-type multiphase lattice boltzmann models. Phys. Rev. E 84 (4), 046710.
Kang, Q., Zhang, D., Chen, S., 2002. Displacement of a two-dimensional immiscible droplet in a channel. Phys. Fluids (1994-present) 14 (9), 3203–3214.
Kang, Q., Zhang, D., Chen, S., 2005. Displacement of a three-dimensional immiscible droplet in a duct. J. Fluid Mech. 545, 41–66.
Lallemand, P., Luo, L.-S., 2000. Theory of the lattice boltzmann method: dispersion, dissipation, isotropy, galilean invariance, and stability. Phys. Rev. E 61 (6), 6546.
Lamb, H., 1932. Hydrodynamics. Cambridge university press.
Li, Q., Luo, K., 2013. Achieving tunable surface tension in the pseudopotential lattice boltzmann modeling of multiphase flows. Phys. Rev. E 88 (5), 053307.
Li, Q., Luo, K., Li, X., 2012. Forcing scheme in pseudopotential lattice boltzmann model for multiphase flows. Phys. Rev. E 86 (1), 016709.
Li, Q., Luo, K., Li, X., 2013. Lattice boltzmann modeling of multiphase flows at large density ratio with an improved pseudopotential model. Phys. Rev. E 87 (5), 053301.
Li, Q., Luo, K., Kang, Q., Chen, Q., 2014. Contact angles in the pseudopotential lattice boltzmann modeling of wetting. Phys. Rev. E 90 (5), 053301.
Liu, X., Cheng, P., Quan, X., 2014. Lattice boltzmann simulations for self-propelled jumping of droplets after coalescence on a superhydrophobic surface. Int. J. Heat Mass Transfer 73, 195–200.

Martys, N.S., Chen, H., 1996. Simulation of multicomponent fluids in complex three-dimensional geometries by the lattice boltzmann method. Phys. Rev. E 53 (1), 743.
Miller, C., Scriven, L., 1968. The oscillations of a fluid droplet immersed in another fluid. J. Fluid Mech. 32 (03), 417–435.
Premnath, K.N., Abraham, J., 2007. Three-dimensional multi-relaxation time (mrt) lattice-boltzmann models for multiphase flow. J. Comput. Phys. 224 (2), 539–559.
Qian, Y., d'Humières, D., Lallemand, P., 1992. Lattice bgk models for Navier–Stokes equation. Europhys. Lett. 17 (6), 479.
Raiskinmäki, P., Koponen, A., Merikoski, J., Timonen, J., 2000. Spreading dynamics of three-dimensional droplets by the lattice-boltzmann method. Comput. Mater. Sci. 18 (1), 7–12.
Sbragaglia, M., Benzi, R., Biferale, L., Succi, S., Toschi, F., 2006. Surface roughness-hydrophobicity coupling in microchannel and nanochannel flows. Phys. Rev. Lett. 97 (20), 204503.
Sbragaglia, M., Benzi, R., Biferale, L., Succi, S., Sugiyama, K., Toschi, F., 2007. Generalized lattice boltzmann method with multirange pseudopotential. Phys. Rev. E 75 (2), 026702.
Sethian, J., Smereka, P., 2003. Level set methods for fluid interfaces. Ann. Rev. Fluid Mech. 35 (1), 341–372.
Shan, X., 2006. Analysis and reduction of the spurious current in a class of multiphase lattice boltzmann models. Phys. Rev. E 73 (4), 047701.
Shan, X., 2008. Pressure tensor calculation in a class of nonideal gas lattice boltzmann models. Phys. Rev. E 77 (6), 066702.
Shan, X., Chen, H., 1993. Lattice boltzmann model for simulating flows with multiple phases and components. Phys. Rev. E 47 (3), 1815.
Shan, X., Chen, H., 1994. Simulation of nonideal gases and liquid–gas phase transitions by the lattice boltzmann equation. Phys. Rev. E 49 (4), 2941.
Succi, S., 2015. Lattice boltzmann 2038. Europhys. Lett. 109 (5), 50001–50007.
Swift, M.R., Osborn, W., Yeomans, J., 1995. Lattice boltzmann simulation of nonideal fluids. Phys. Rev. Lett. 75 (5), 830.
Swift, M.R., Orlandini, E., Osborn, W., Yeomans, J., 1996. Lattice boltzmann simulations of liquid–gas and binary fluid systems. Phys. Rev. E 54 (5), 5041.
Unverdi, S.O., Tryggvason, G., 1992. A front-tracking method for viscous, incompressible, multi-fluid flows. J. Comput. Phys. 100 (1), 25–37.
Yuan, P., Schaefer, L., 2006. Equations of state in a lattice boltzmann model. Phys. Fluids (1994-present) 18 (4), 042101.